J Mater Sci: Mater Electron (2021) 32:20252–20258

Tunable optoelectronic properties of a two-dimensional graphene/α-In_2Se_3/graphene-based ferroelectric semiconductor field-effect transistor

Abdelkader Abderrahmane[1], Changlim Woo[1], and Pil Ju Ko[1,*]

[1] *Department of Electrical Engineering, Chosun University, 375, Seosuk-dong, Dong-gu, Gwangju 501-759, Republic of Korea*

Received: 12 March 2021
Accepted: 29 June 2021
Published online: 6 July 2021

ABSTRACT

Two-dimensional (2D) materials are promising for future electronic and optoelectronic devices. In particular, 2D material-based photodetectors have been widely studied because of their excellent photodetection performance. Owing to its excellent electrical and optical characteristics, 2D indium selenide (α-In_2Se_3) is a good candidate for photodetection applications. In addition, α-In_2Se_3 samples, including atom-thick α-In_2Se_3 layers, present ferroelectric properties. Herein, we report the fabrication and electrical and optoelectronic properties of multilayered graphene (Gr)/α-In_2Se_3/Gr-based ferroelectric semiconductor field-effect transistors (FeS-FETs). Furthermore, we discuss the physical mechanisms affecting electronic and optoelectronic transport in the Gr/α-In_2Se_3/Gr heterostructure. Large hysteresis was observed in the transfer characteristic curves and it was attributed to the ferroelectric polarization of MTL α-In_2Se_3 and carrier trapping–detrapping effects. The optoelectronic performance of the fabricated FeS-FETs depended on the ferroelectric properties of α-In_2Se_3 and can be easily tuned to achieve the maximum photoresponsivity and specific detectivity of 10 AW^{-1} and 4.4 × 10^{12} $cmHz^{1/2}$ W^{-1}, respectively.

1 Introduction

Indium selenide (α-In_2Se_3) is a III_2–VI_3 binary chalcogenide material with a bandgap in the range of 1.39–1.45 eV [1]. The excellent electrical and optical properties of α-In_2Se_3 render it a good candidate for photodetection applications [2–5]. Moreover, α-In_2Se_3 samples, including atom-thick α-In_2Se_3 layers, exhibit ferroelectric properties at room temperature. Ding et al. [6] reported that α-In_2Se_3 exhibited a spontaneous polarization that can be reoriented using an external electric field; therefore, α-In_2Se_3 is suitable for memory devices and applications, such as solar cells and photovoltaics [1], wide-range photodetectors [7], neuromorphic computing systems [8], and photocatalytic water splitting devices [9]. Recently, Si et al. [10] have fabricated a ferroelectric semiconductor field-effect transistor (FeS-FET)-based memory device using two-dimensional (2D) α-In_2Se_3 and have utilized it to address the shortcomings of

Address correspondence to E-mail: pjko@chosun.ac.kr

https://doi.org/10.1007/s10854-021-06528-8

non-destructive ferroelectric field-effect transistors featuring ferroelectric materials as gate insulators, such as short retention times, charge trapping, and current leaking through the ferroelectric insulator.

In this study, we fabricated a new FeS-FET device based on multilayered (MTL) graphene (Gr) as the drain and source contacts and 2D MTL α-In_2Se_3 as the channel (Gr/α-In_2Se_3/Gr) and analyzed its electrical properties and the physical mechanisms affecting the electronic and optoelectronic transport in the device. The effects of the ferroelectric nature of α-In_2Se_3 and trapping–detrapping on the optoelectronic performance of the photodetector are discussed herein. The maximum photoresponsivity and specific detectivity of the Gr/α-In_2Se_3/Gr-based FeS-FET-based photodetector were 10 AW^{-1} and 4.4×10^{12} $cmHz^{1/2}W^{-1}$, respectively, which indicated the high performance of the device for photodetection applications.

2 Experimental section

2.1 Experimental details

The Gr/α-In_2Se_3/Gr-based FeS-FET-based photodetector was fabricated using a mechanical exfoliation technique. Gr and α-In_2Se_3, were purchased from HQ Graphene and were first mechanically exfoliated onto polydimethylsiloxane (PDMS) (Dow Corning, Toray Co., Ltd). Then, MTL Gr contacts were deposited using PDMS on 50 nm titanium electrodes that were deposited by electron beam evaporation. Thereafter, the MTL 2D α-In_2Se_3 nanosheet was transferred from PDMS by mechanical exfoliation technique on the MTL Gr contacts. A p-type Si substrate with a 300 nm thick silicon dioxide (SiO_2) layer was used as the dielectric gate insulator.

2.2 Characterization techniques

Park NX20 atomic force microscope (AFM) and JEOLJSM-7500F + EDS(Oxford) were used for morphological and topographic analysis characterizations. The electrical and optoelectronic properties of the device were evaluated using a Keithley 4200A-SCS parameter analyzer and mobiken laser power meter LP1 was used for power light calibration prior the experiments. The laser power(P) ranged between 0.016 and 1.55 μW, and the wavelength and laser spot diameter were 532 nm and 20 mm, respectively.

3 Results and discussion

3.1 Morphological analysis

The schematic diagram and corresponding scanning electron micrograph of the fabricated device are presented in Fig. 1a and b, respectively. The length of the channel between the MTL Gr contacts was estimated to be 12 μm. The atomic force microscopy images of the MTL materials are illustrated in Fig. 1c. Topographic analysis revealed that the thicknesses of the drain MTL Gr contacts, MTL In_2Se_3, and source MTL Gr contacts were 125, 160, and 60 nm, respectively (Fig. 1d).

3.2 Electrical characterization

The drain current (I_{DS}) dependence on the drain-source voltage (V_{DS}) at different gate-source voltages (V_{GS}) of the Gr/α-In_2Se_3/Gr-based FeS-FET heterostructure wherein the MTL Gr contacts present a Schottky barrier is illustrated in Fig. 2a. Under a negative back-gate voltage (V_{BG}), the electronic transport was dominated by minority carriers, resulting in a low I_{DS}. However, when V_{BG} exceeded the flat-band voltage, both types of carriers (holes in the valence band and electrons in the conduction band) were involved in electronic transport, resulting in high I_{DS} values. I_{DS} increased as V_{BG} increased from − 10 to 40 V (Fig. 2a, inset), confirming the n-type and normally off behavior of the device. The hysteresis observed in the inset of Fig. 2a is explained in the last section of this paper. The I_{DS}–V_{DS} characteristics of the Gr/α-In_2Se_3/Gr device at different P values are presented in Fig. 2b. I_{DS} increased with increasing P owing to the increase in number of photogenerated carriers in MTL α-In_2Se_3.

3.3 Optoelectronic characterization

The dependence of the optoelectronic properties of the Gr/α-In_2Se_3/Gr device on the V_{BG} applied along the vertical direction of the Cu/p-Si/SiO_2/α-In_2Se_3 structure are illustrated in Fig. 3a–d. The transfer characteristic curves of the Gr/α-In_2Se_3/Gr device at different P values are presented in Fig. 3a.

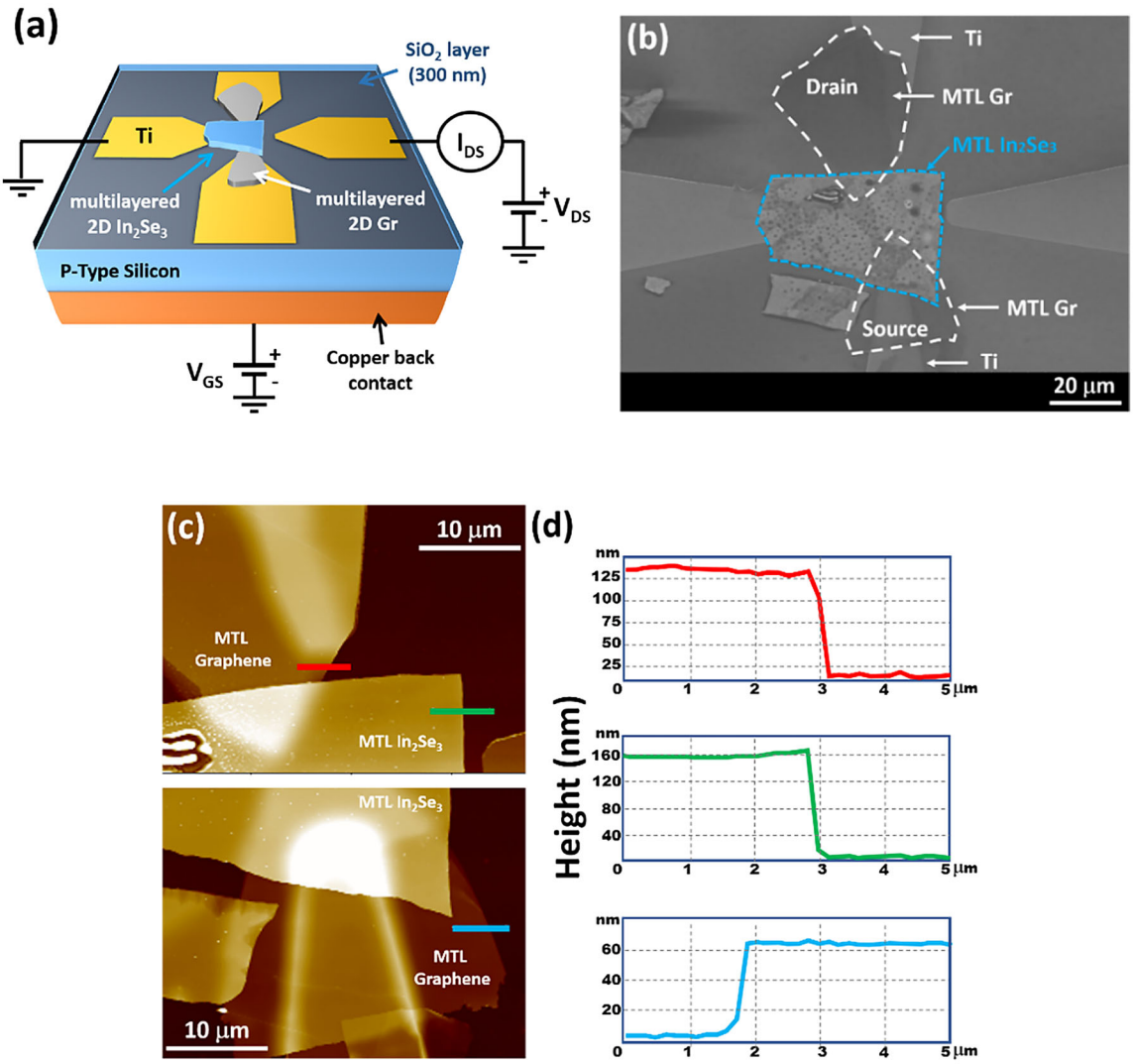

Fig. 1 **a** Schematic diagram and **b** scanning electron micrograph of the of the fabricated multilayered (MTL) graphene Gr/α-In_2Se_3/Gr device. **c** Atomic force microscopy images of MTL Gr and α-In_2Se_3. **d** Thicknesses of the two-dimensional drain MTL Gr contacts (red), MTL In_2Se_3 (green), and source MTL Gr (blue) contacts determined using topographic analysis. Here, I_{DS}, V_{DS}, and V_{GS} denote drain current, drain-source voltage, and gate-source voltage, respectively (Color figure online)

The photocurrent (I_{PH}) was measured by the difference between the I_{DS} values under light irradiation and in the dark. I_{PH} increased with increasing P owing to the increase in density of the photoexcited carriers (Fig. 3b); moreover, I_{PH} did not reach saturation. The dependence of photoresponsivity (R_λ), which was calculated as follows: $R_\lambda = I_{PH}/P$, on V_{BG} is illustrated in Fig. 3c. R_λ increased with increasing V_{BG} because I_{PH} increased, and decreased with increasing P. The specific detectivity (D^*) represents the capability of FeS-FETs to detect weak signals, and can be calculated as follows: $D^* = R_\lambda \times A^{1/2}/(2 \times e \times I_{\mathrm{dark}})^{1/2}$, where I_{dark}, the current in the dark, is the main contributor to shot noise, A is the effective irradiation area, and e is the electron charge. D^* increased to a maximum of 1.77×10^{12} cmHz$^{1/2}$ W^{-1} when V_{DS} and V_{BG} were 1 and 5 V, respectively and decreased when V_{BG} exceeded 5 V. A detailed explanation of the changes in R_λ and D^* with the forward and reverse I_{DS} is included in the last section of the paper (Fig. 5).

The I_{DS}–V_{BG} transfer characteristic curves in the forward and reverse directions, when V_{BG} increased from − 10 to 40 V and then decreased back to − 10 V are presented in Fig. 4a. I_{DS} presented a clockwise hysteresis loops in the dark and under laser

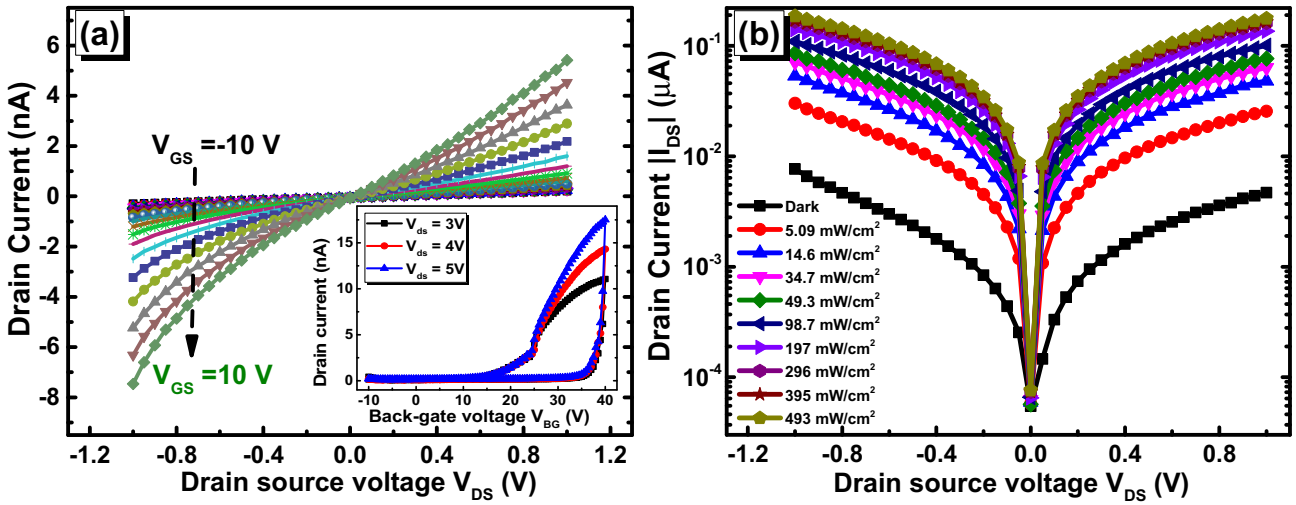

Fig. 2 **a** Drain current (I_{DS})–drain-source voltage (V_{DS}) diagrams of the Gr/α-In_2Se_3/Gr device at different gate-source voltages (V_{GS}). The transfer characteristic curves of the Gr/α-In_2Se_3/Gr device at V_{DS} of 3, 4, and 5 V are included in the inset. **b** I_{DS}–V_{DS} characteristics at different laser power densities. Here V_{BG} denotes back-gate voltage

irradiation. Other 2D material-based FETs, such as MoS_2 [11] and WSe_2 [12], exhibited electrical hysteresis; however, α-In_2Se_3 presented a wider memory window than MoS_2 and WSe_2 (Fig. 4a). Si et al. [10] attributed the electrical hysteresis of α-In_2Se_3 to the ferroelectric polarization of the α-In_2Se_3 layer. Furthermore, Li et al. [13] ascribed the large memory window of α-In_2Se_3 to its high charge capturing capability. To better understand the physical mechanism affecting the electronic and optoelectronic transports in forward and reverse directions, we drew the band diagrams of the Gr/α-In_2Se_3/Gr device along the vertical direction of the Cu/p-Si/SiO_2/α-In_2Se_3 system (Fig. 4c). The bandgap energy, work function, and electron affinity of α-In_2Se_3 were 1.4 eV [14], 4.35 eV [15], and 3.6 eV [16], respectively (Fig. 4c-i). At equilibrium, a depletion region formed at the SiO_2–α-In_2Se_3 interface (Fig. 4c-ii), that is, the Gr/α-In_2Se_3/Gr device was normally off in the depletion regime. When a very low negative V_{BG} was applied to the Gr/α-In_2Se_3/Gr device (Fig. 4c-iii), electrons were injected from the electron traps at the SiO_2–α-In_2Se_3 interface into the conduction channel. In addition, the electrical dipole in the α-In_2Se_3 layer was polarized in the downward direction, which pushed electrons from the surface of the α-In_2Se_3 layer into its bulk (Fig. 4c-iii). In general, traps in α-In_2Se_3 are ascribed to the natural oxide layer at the α-In_2Se_3–SiO_2 interface [17] and the adsorption of water and oxygen molecules at the α-In_2Se_3 surface [13, 18]. Therefore, the threshold V_{BG} shifted to negative values in the forward direction owing to an increase in electron density.

Nevertheless, by increasing V_{BG} to positive values (Fig. 4c-iv), electrons, which were the majority charge carriers accumulated at the SiO_2–α-In_2Se_3 interface and I_{DS} increased. In this case, the electrical dipole in the α-In_2Se_3 layer was polarized in the upward direction. Therefore, electrons were pushed toward the surface far from the conduction layer; moreover, because V_{BG} was positive, electrons started to fill the electron traps at the SiO_2–α-In_2Se_3 interface. Consequently, in reverse mode (Fig. 4c-v), fewer electrons were available for electronic transport, and the threshold voltage shifted to positive values.

Under light illumination, the concentration of charge carriers in α-In_2Se_3 increased owing to the generation of electron–hole pairs, which increased I_{PH} and shifted the threshold voltage in the negative direction (Fig. 4b). Conversely, under light excitation, electrons were removed from the trap states at the SiO_2–α-In_2Se_3 interface and the α-In_2Se_3 surface and were injected into the conduction band of α-In_2Se_3. Because electron detrapping occurred in reverse mode, the threshold voltage shifted more toward the negative values of V_{BG} and increased with increasing P, which explained hysteresis (or memory window) narrowing.

The hysteresis loops of α-In_2Se_3 strongly affect its optoelectronic properties. R_λ presented clockwise

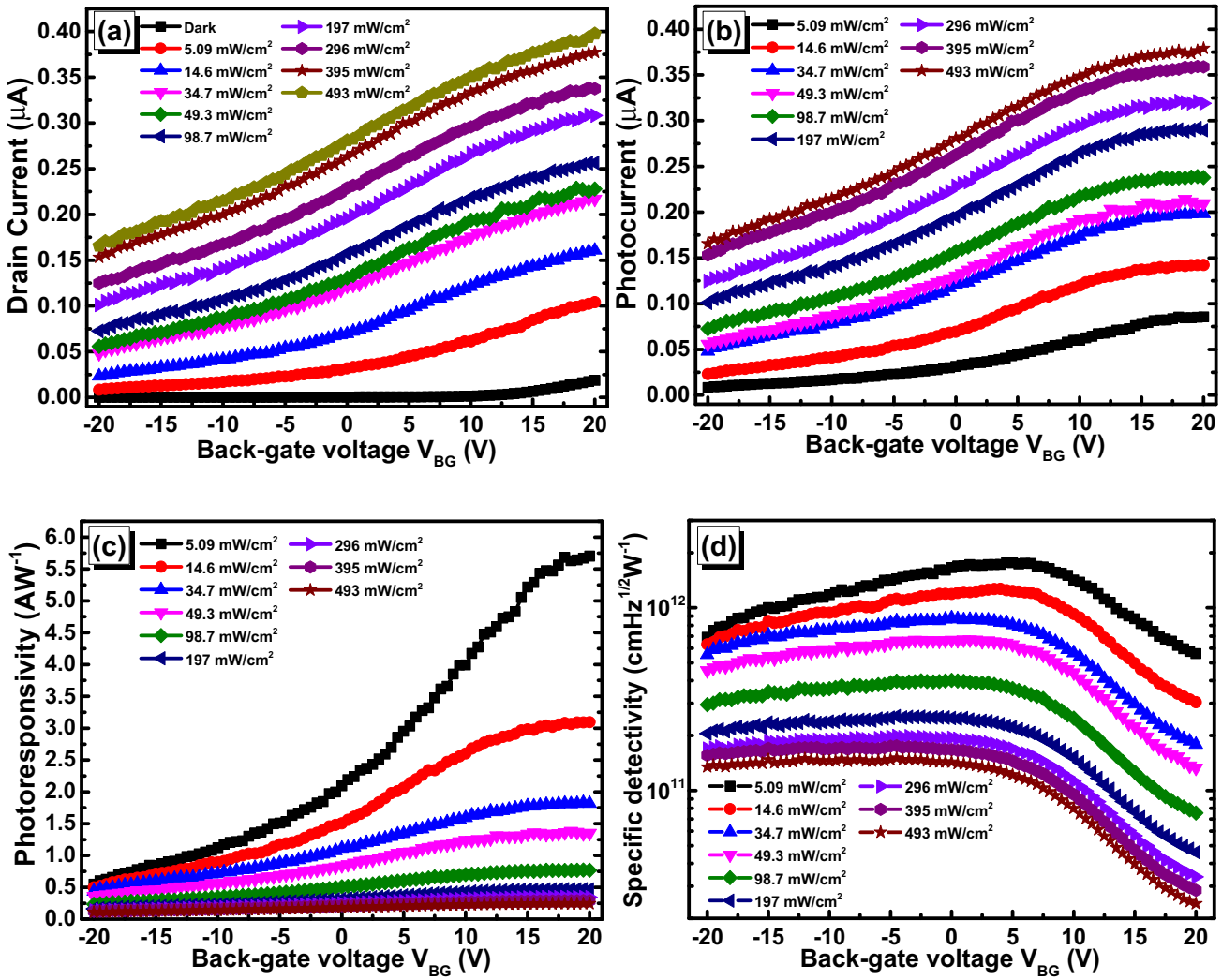

Fig. 3 **a** Drain current (I_{DS})–back-gate voltage (V_{BG}) transfer characteristic curves of the of graphene (Gr)/α-In_2Se_3/Gr-based ferroelectric semiconductor field-effect transistor in the dark and at different laser power densities and **b** photocurrent (I_{PH}), **c** photoresponsivity (R_λ), and **d** specific detectivity (D^*) dependence on V_{BG} at different laser power densities, at V_{DS} of 1 V

hysteresis with a maximum value of 10 AW^{-1} when V_{BG} exceeded 30 V (Fig. 5a). R_λ decreased with increasing P from 0.016 to 0.93 μW owing to trapping–detrapping effects. Similarly, D^* presented a pinched hysteresis loop (Fig. 5b). D^* increased to 4.4×10^{12} $cmHz^{1/2}$ W^{-1} when V_{DS} and V_{BG} were 5 and 35 V, respectively. The pinched loop hysteresis of D^* was attributed to the decrease in D^* at high V_{BG} values, which was caused by the exponential increase in I_{dark} (insets of Figs. 2a and 4a).

4 Conclusion

In summary, we fabricated a new MTL Gr/α-In_2Se_3/Gr-based FeS-FET, analyzed its electrical and optoelectronic properties, and investigated the physical mechanisms responsible for tuning its optoelectronic performance. The large hysteresis observed in the transfer characteristic curves of the Gr/α-In_2Se_3/Gr device was attribute to the ferroelectric polarization of MTL α-In_2Se_3 and carrier trapping–detrapping

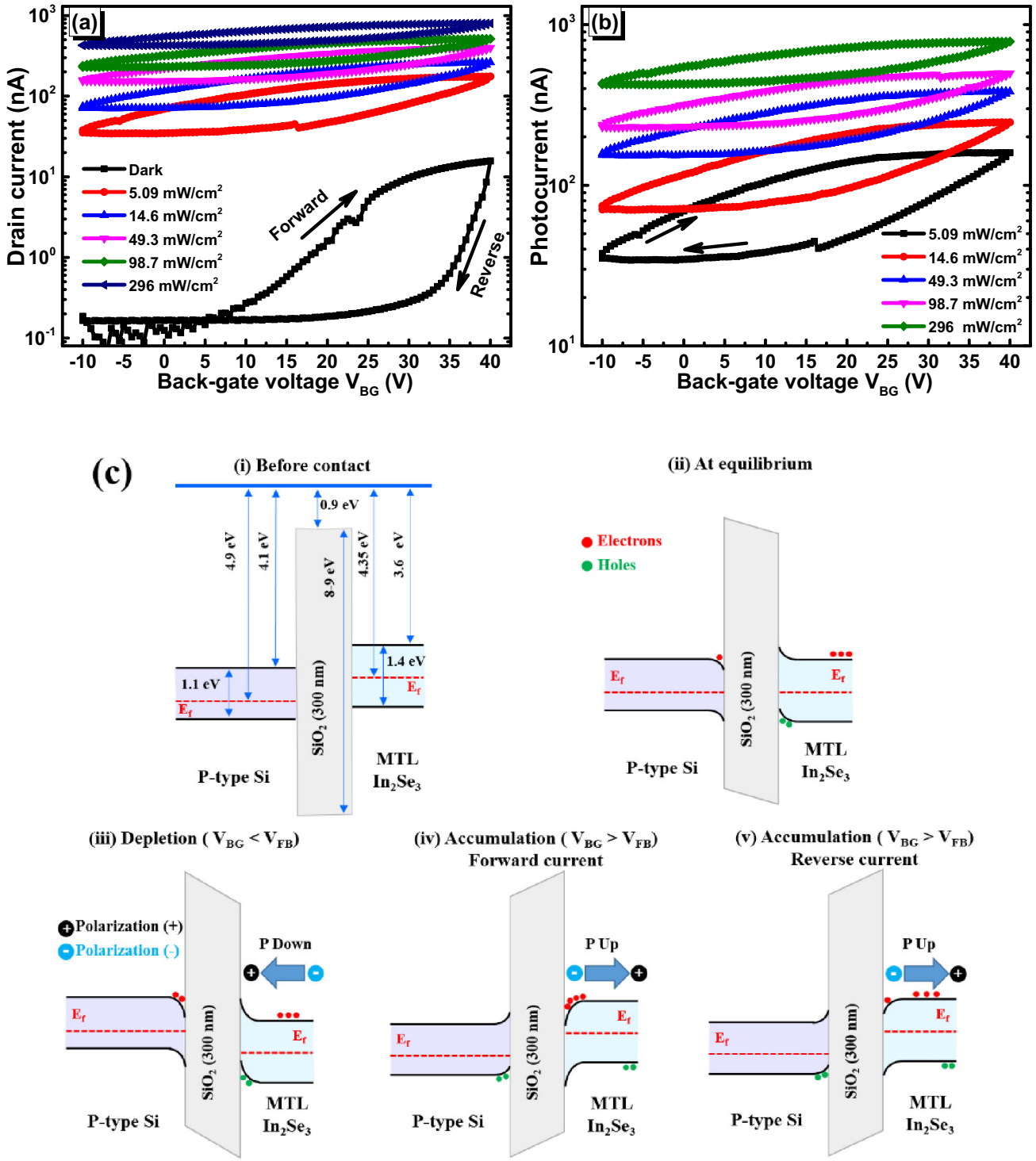

Fig. 4 Dependence of **a** drain current (I_{DS}) and **b** photocurrent (I_{PH}) on the back-gate voltage (V_{BG}) and laser power density in the forward and reverse directions, at V_{DS} of 5 V. **c** Band diagrams of the Gr/α-In_2Se_3/Gr device in the vertical direction at different operating conditions illustrating the effect of the electrical dipole polarization on electronic transport. Here Gr and MTL denote graphene and multilayered, respectively, and V_{FB} and E_f denote flat-band voltage, and Fermi energy level, respectively

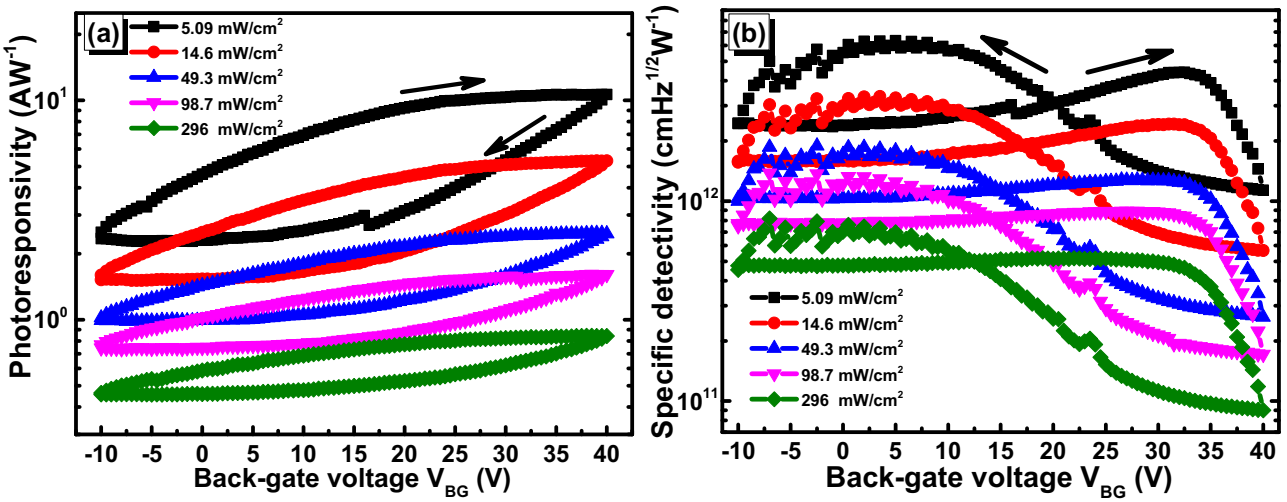

Fig. 5 Dependence of **a** photoresponsivity (R_λ) and **b** specific detectivity (D^*) on the back-gate voltage (V_{bg}) and laser power density in the forward and reverse directions, at V_{DS} of 5 V

effects. The maximum R_λ and D^* values of the Gr/α-In_2Se_3/Gr device were 10 AW^{-1} and 4.4×10^{12} $cmHz^{1/2}\,W^{-1}$, respectively, confirming that the Gr/α-In_2Se_3/Gr-based FeS-FET photodetector can be a promising device for photodetection applications.

Acknowledgements

This work was supported by Brain Pool Program through the National Research Foundation of Korea (NRF) funded by the Ministry of Science and ICT [Grant Number NRF-2019H1D3A1A01102658].

References

1. R.K. Mech, N. Mohta, A. Chatterjee, S.K. Selvaraja, R. Muralidharan, D.N. Nath, Phys. Status Solidi A **217**(5), 1900932 (2020)
2. Z. Zhang, J. Yang, F. Mei, G. Shen, Front. Optoelectron. **11**(3), 245–255 (2018)
3. B. Liu, B. Tang, F. Lv, Y. Zeng, J. Liao, S. Wang, Q. Chen, Nanotechnology **31**(6), 065203 (2019)
4. P. Hou, Y. Lv, X. Zhong, J. Wang, ACS Appl. Nano Mater. **2**(7), 4443–4450 (2019)
5. W. Li, M. Dai, Y. Hu, H. Chen, X. Zhu, Q. Yang, P. Hu, ACS Appl. Nano Mater. Interfaces **11**(50), 47098–47105 (2019)
6. W. Ding, J. Zhu, Z. Wang, Y. Gao, D. Xiao, Y. Gu, Z. Zhang, W. Zhu, Nat. Commun. **8**(1), 1–8 (2017)
7. S.V. Solanke, R. Soman, M. Rangarajan, S. Raghavan, D.N. Nath, Sens. Actuator A **317**, 112455 (2021)
8. L. Wang, X. Wang, Y. Zhang, R. Li, T. Ma, K. Leng, Z. Chen, I. Abdelwahab, K.P. Loh, Adv. Funct. Mater. **30**(45), 2004609 (2020)
9. E.F. Procopio, R.N. Pedrosa, F.A. de Souza, W.S. Paz, W.L. Scopel, Phys. Chem. Chem. Phys. **22**(6), 3520–3526 (2020)
10. M. Si, A.K. Saha, S. Gao, G. Qiu, J. Qin, Y. Duan, J. Jian, C. Niu, H. Wang, W. Wu, S.K. Gupta, Nat. Electron. **2**(12), 580–586 (2019)
11. N. Kaushik, D.M. Mackenzie, K. Thakar, N. Goyal, B. Mukherjee, P. Boggild, D.H. Petersen, S. Lodha, NPJ 2D Mater. Appl. **1**(1), 1–9 (2017)
12. N. Oliva, Y.Y. Illarionov, E.A. Casu, M. Cavalieri, T. Knobloch, T. Grasser, A.M. Ionescu, IEEE J. Electron Devices Soc. **7**, 1163–1169 (2019)
13. Q. Li, C. Yuan, T. Yu, Q. Wang, J. Li, J. Phys. D **53**(7), 075108 (2019)
14. J.R. Rodriguez, W. Murray, K. Fujisawa, S.H. Lee, A.L. Kotrick, Y. Chen, N. Mckee, S. Lee, M. Terrones, S. Trolier-McKinstry, T.N. Jackson, Appl. Phys. Lett. **117**(5), 052901 (2020)
15. S. Sakalauskas, A. Sodeika, Rev. Sci. Instrum. **69**(2), 466–468 (1998)
16. S.I. Drapak, Z.D. Kovalyuk, V.V. Netyaga, V.B. Orletskii, Tech. Phys. Lett. **28**(9), 707–710 (2002)
17. J.O. Island, S.I. Blanter, M. Buscema, H.S. van der Zant, A. Castellanos-Gomez, Nano Lett. **15**(12), 7853–7858 (2015)
18. C.H. Ho, C.H. Lin, Y.P. Wang, Y.C. Chen, S.H. Chen, Y.S. Huang, ACS Appl. Mater. Interfaces **5**(6), 2269–2277 (2013)